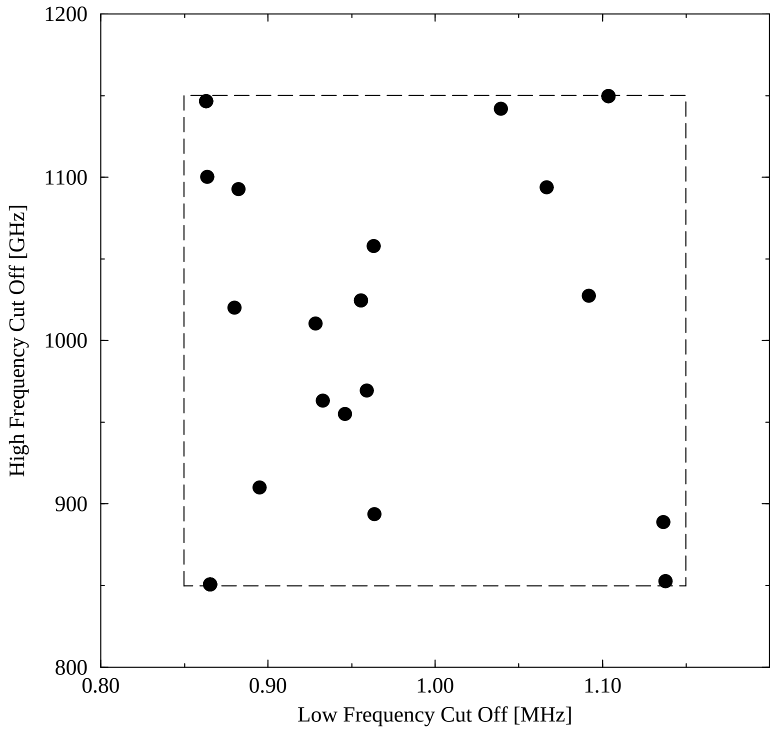

Figure 4.13: Distribution of the low– and high–frequency cutoffs corresponding to the best fits to the multifrequency datasets. Dashed line indicates the ranges of allowed cutoff variation.

By varying the spectral dataset, we then produce *simulated datasets*

$$S_{sym} = \mathcal{V}(S_s)|_{\{\sigma^2_S(\nu)\}} \tag{4.13}$$

assuming the Gaussian distribution of the errors in flux density measurements

$$\phi(S) = \frac{1}{\sqrt{2\pi}\sigma_\nu} e^{-1/2\left(\frac{S-S_\nu}{\sigma_\nu}\right)^2} \tag{4.14}$$

where S_ν and σ_ν are the measured flux density and its variance.

For each simulated dataset we apply the M–order polynomial fitting by the basis functions $X_k(\nu) = \nu^k$, and minimize the χ^2 parameter of the fit

$$\chi^2 = \sum_{i=1}^{N} \frac{1}{\sigma_i^2} \left[(S_{sym})_i - \sum_{k=0}^{M} A_k X_k(\nu_i) \right]^2, \tag{4.15}$$

to obtain the least squares fit to the data

$$\sum_{j=0}^{M} \alpha_{j,k} A_j = \beta_k; \quad \alpha_{j,k} = \sum_{i=1}^{N} \frac{X_j(\nu_i) X_k(\nu_i)}{\sigma_i^2}, \quad \beta_k = \sum_{i=1}^{N} \frac{(S_{sym})_i X_k(\nu_i)}{\sigma_i^2}, \tag{4.16}$$

and derive the polynomial coefficients

$$A_j = \sum_{k=0}^{M} [\alpha]^{-1}_{jk} \beta_k, \quad \sigma^2(A_j) = [\alpha]{-1}_{jj} \tag{4.17}$$

From the fit to the spectral dataset, we derive the basic parameters of the synchrotron spectrum: the integrated flux S_{int},

$$S_{int} = \int_{\nu_L}^{\nu_H} \sum_{j=0}^{M} A_j \nu^j d\nu \tag{4.18}$$

the turnover frequency ν_m, and the maximum flux density S_m

$$\frac{d\sum_{j=0}^{M} A_j \nu^j}{d\nu} = 0 \;\Rightarrow\; S_m, \nu_m \tag{4.19}$$

We then analyze the distribution of the χ^2 parameters from the fits to all simulated datasets. From this analysis, standard deviations at the 3σ confidence level are calculated for S_{int}, S_m, and ν_m.

4.3.5 Analysis of multifrequency data

Since, typically, VLBI observations at different frequencies have not been made simultaneously, for our analysis we select the observing epochs which are relatively close in time, so that source variability will not significantly contaminate the multifrequency analysis. Inspecting the light curves for the total flux and the fluxes of individual components yields a time interval of up to 6 months during which the flux changes do not exceed the flux errors of the model fitting. We use this criterion to combine the flux data into *multifrequency datasets*. Choosing stricter limitations on time proximity would result in too few possibilities available to construct a multifrequency dataset.

The multifrequency datasets are summarized in Table 4.6. Every multifrequency dataset, except for the first two, contains observations at three or more frequencies. However, if a component was not detected at one of the frequencies at a given epoch, the corresponding dataset for this component may contain data at only two frequencies. In the latter case, the spectral fit is determined by the spectral index between the two frequencies. In this case, the uncertainties of the fit parameters increase substantially, and we down–weighted these values in the subsequent analysis.

For the fit, we assume self–absorbed synchrotron emission from a relativistic plasma with a power–law energy distribution to dominate the source spectrum on VLBI spatial scales (see Section 4.3.1). Based on this assumption, we determine the shape of the synchrotron spectrum of the jet via the following two steps:

1. We apply third order polynomial fits to the multifrequency datasets with the cutoff information included. In order to achieve the best fit, the *loose–cutoff* method is implemented: the cutoff frequencies are allowed to vary by 15%, and those values providing the lowest χ^2 parameter of the fit have been selected. The distribution of the cutoff values determined by this method is presented in Figure 4.13. The cutoffs do not show a systematic trend, and are not concentrated along the 15% offset boundaries, thus reassuring validity of the initial estimate of the cutoffs. A

Table 4.6: VLBI and total fluxes of the datasets.

(1) Epoch	(2) ν	(3) S_{VLBI}	(4) σ_{VLBI}	(5) S_{tot}	(6) σ_{tot}	(7) Ref.
1979.250	4.99	7.500	0.412	...	...	1
1979.440	10.70	8.530	1.281	8.59	0.14	1
1980.520	10.70	10.480	1.928	10.13	0.10	1
1980.730	4.99	7.400	0.151	8.02	0.05	1
1981.090	10.70	12.830	1.237	13.01	0.60	1
1981.250	22.30	13.870	0.304	14.92	0.77	1
1981.630	4.99	9.890	0.168	10.08	0.05	1
1982.090	10.70	15.190	0.534	15.34	0.32	1
1982.380	89.20	12.000	6.403	13.47	8.62	3
1982.560	4.99	10.670	0.297	11.35	0.07	1
1983.090	22.30	13.200	0.900	15.01	0.28	1
1983.100	10.70	14.660	1.057	14.67	0.26	1
1983.570	4.99	9.520	0.871	11.44	0.15	1
1984.090	22.30	13.200	0.640	13.87	0.23	1
1984.110	10.70	13.740	0.842	14.12	0.31	1
1984.252	4.99	7.429	0.378	12.80	0.12	2
1985.750	22.30	6.362	0.182	10.90	0.28	2
1985.769	4.99	9.246	0.244	11.52	0.06	2
1985.934	10.70	9.880	0.724	11.44	0.79	2
1986.901	4.99	10.012	0.822	10.56	0.08	2
1987.151	10.70	9.474	0.157	11.03	0.48	2
1987.424	22.30	3.930	0.105	9.32	0.21	2
1988.159	22.30	5.070	0.088	7.73	0.18	2
1988.167	10.70	8.699	0.781	8.86	0.52	2
1988.178	4.99	7.845	0.122	9.52	0.09	2
1988.210	100.00	3.200	0.854	...	...	4
1989.220	100.00	3.200	0.520	...	...	4
1989.246	22.30	5.980	0.297	5.89	0.21	8
1989.262	10.70	7.527	0.562	7.01	0.33	8
1989.280	4.99	7.846	0.448	8.06	0.06	5
1990.164	10.70	3.141	0.157	5.81	0.03	7
1990.180	4.99	6.495	0.351	6.56	0.06	5
1990.420	22.30	3.012	0.223	5.92	0.20	7
1990.490	43.20	7.876	0.763	5.04	0.45	6

(continued on the next page)

Table 4.6: (continued)

(1) Epoch	(2) ν	(3) S_{VLBI}	(4) σ_{VLBI}	(5) S_{tot}	(6) σ_{tot}	(7) Ref.
1991.680	43.20	22.700	4.545	...	...	6
1991.710	4.99	4.969	0.825	5.24	0.05	5
1991.863	22.30	12.104	0.719	12.36	0.28	8
1992.427	4.99	6.609	0.744	6.43	0.04	8
1992.449	22.30	13.231	2.043	11.97	0.43	8
1992.712	8.40	10.589	4.083	10.35	0.15	8
1993.695	4.99	6.416	0.460	8.15	0.06	8
1993.723	22.30	6.145	0.156	8.53	0.31	8
1993.887	8.40	8.477	0.199	9.99	0.19	8

Notes: 1–epoch; 2–frequency[GHz]; 3–VLBI flux[Jy]; 4–VLBI flux error[Jy]; 5–total flux[Jy]; 6–total flux error[Jy]; 7–reference. References: 1–(Biretta *et al.* 1986); 2–(Zensus *et al.* 1995a); 3–(Krichbaum *et al.* 1991); 4–(Krichbaum *et al.* 1991); 5–(Unwin & Wehrle 1992); 6–(Krichbaum *et al.* 1993); 7–(Unwin *et al.*1994); 8–this dissertation.

tendency of the low–frequency cutoff to be lower than the initial value may reflect a bias towards flattening the self–absorbed part of the spectrum.

2. After the optimum cutoff frequencies have been found, we calculate the frequency of the spectral peak ν_m(essentially, the *turnover frequency* as utilized in *e.g.* Marscher *et al.* 1979, Simon *et al.* 1983, Cohen 1985) and the integrated 4–25 GHz flux S_{int}. The uncertainties for these parameters were estimated using a Monte Carlo simulation described in Section 4.3.4 The uncertainties are calculated at the 99% confidence level.

4.3.6 Fitted spectra of the bright components

Figures 4.14–4.17 present the fits for the core D and the components C5, C4, and C3. At lower flux levels, the flux errors are uneven due to the logarithmic representation of the data. The fits are likely to be slightly biased towards steepening the optically thin part of the spectrum and simultaneously flattening the optically thick part of it. Because of this effect, we calculate the integrated flux within 4–25 GHz range of frequencies, so that the influence of the bias would be negligible. Table 4.7 contains the fitted values for ν_m, S_{int} and peak flux density S_{ν_m}.

4.4 Continuous spectral fitting

On the basis of discrete spectral fitting discussed in Section 4.3, we have developed a procedure for fitting the synchrotron spectrum in every pixel, using VLBI images at different frequencies, rather than Gaussian models. Continuous fitting to the syn-

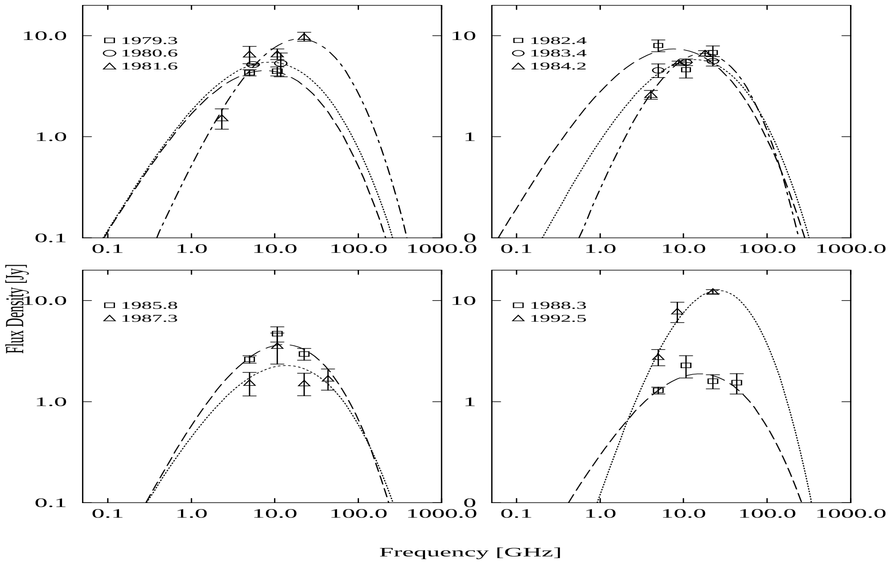

Figure 4.14: Fitted spectra of the VLBI core D. For better viewing, some of the datasets and corresponding fits are slightly shifted.

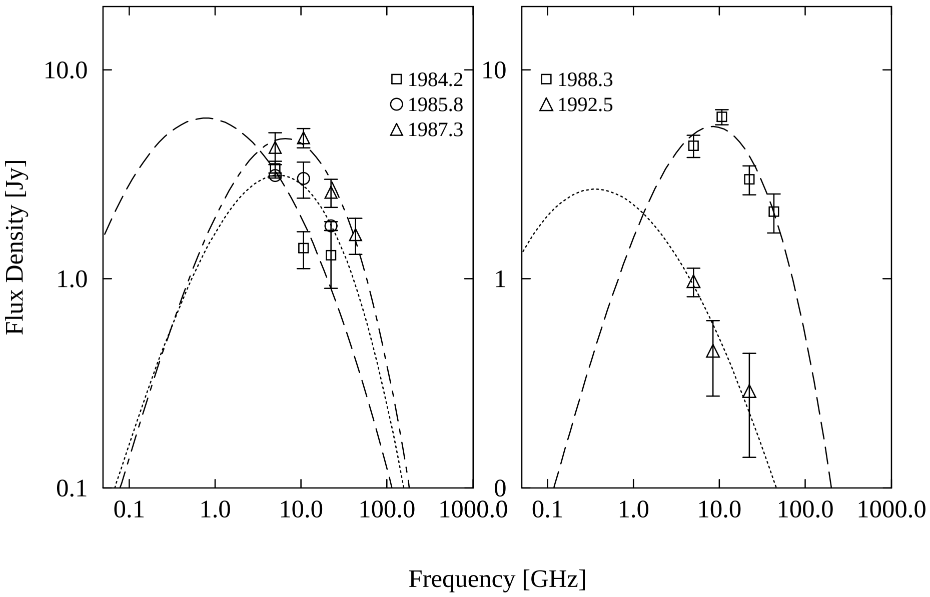

Figure 4.15: Fitted spectra of the component C5.

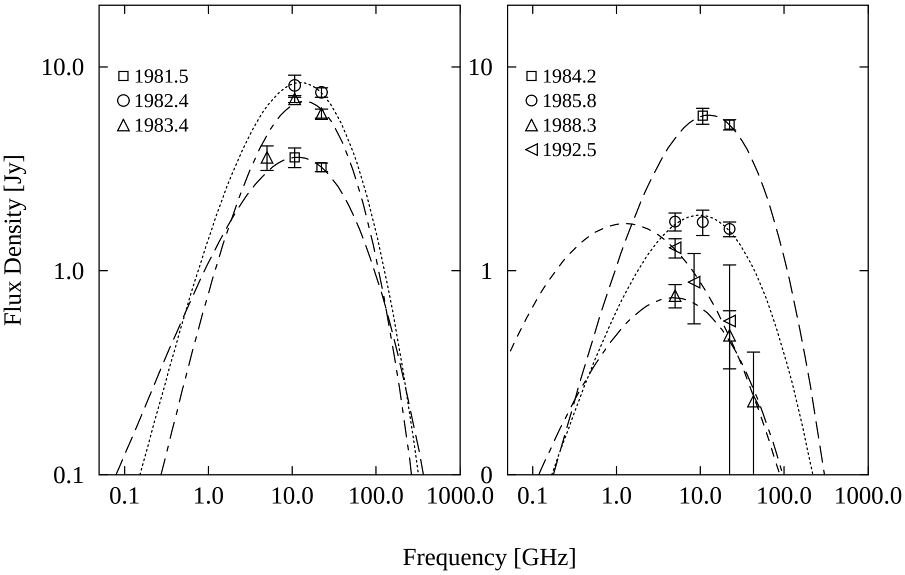

Figure 4.16: Fitted spectra of the component C4.

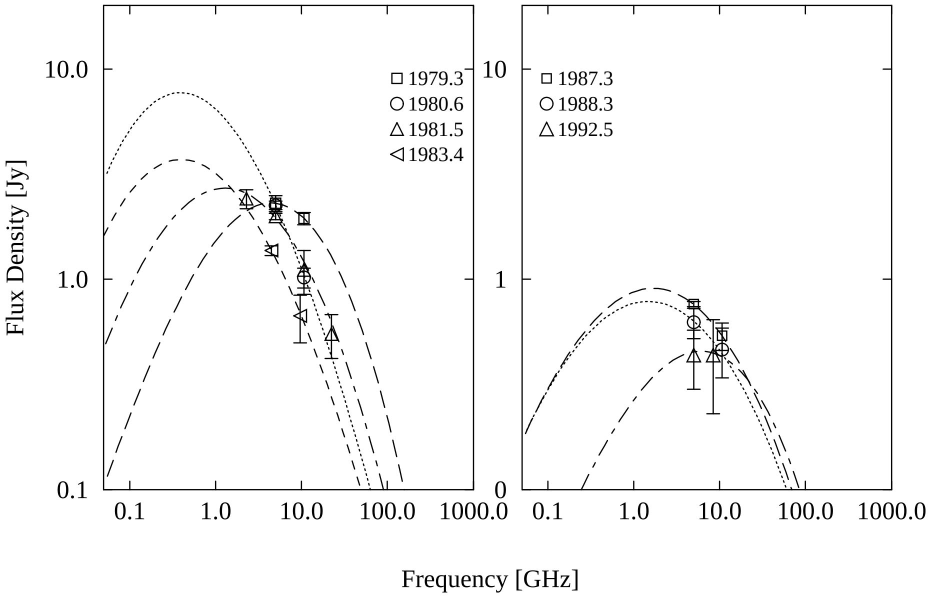

Figure 4.17: Fitted spectra of the component C3.

Table 4.7: Spectral fits.

(1) Name	(2) τ_ν	(3) N_ν	(4) S_{int}	(5) S_m	(6) ν_m	(7) γ_{min}	(8) $L_{max}^{4-25\,GHz}\ h^{-2}$
D	1979.3	2	81.8 ± 3.7	4.5 ± 0.1	7.6 ± 0.8	(3.5)	8.0×10^{42}
	1980.6	2	82.6 ± 3.2	4.4 ± 0.3	6.6 ± 1.8	(3.5)	8.0×10^{42}
	1981.5	3	164.9 ± 8.9	9.3 ± 0.3	20.0 ± 0.7	(3.5)	1.2×10^{43}
	1982.4	3	135.3 ± 7.5	7.4 ± 0.2	7.7 ± 0.6	(3.5)	1.3×10^{43}
	1983.4	3	113.1 ± 5.7	5.8 ± 0.1	13.8 ± 0.8	(3.5)	9.2×10^{42}
	1984.2	3	117.6 ± 6.0	6.7 ± 0.2	21.3 ± 0.5	(3.5)	7.9×10^{42}
	1985.8	3	71.3 ± 2.4	3.7 ± 0.1	12.9 ± 0.5	(3.5)	5.8×10^{42}
	1987.3	3	44.8 ± 1.3	2.3 ± 0.1	13.7 ± 1.2	(3.5)	3.7×10^{42}
	1988.2	4	33.8 ± 1.0	1.9 ± 0.1	15.8 ± 0.6	(3.5)	2.9×10^{42}
	1989.2	4	29.7 ± 1.2	1.5 ± 0.1	12.5 ± 2.9	(3.5)	2.5×10^{42}
	1990.3	4	31.9 ± 1.1	1.6 ± 0.1	17.0 ± 3.4	(3.5)	2.5×10^{42}
	1991.7	3	106.0 ± 4.1	9.4 ± 0.3	41.0 ± 3.2	(3.5)	6.3×10^{42}
	1992.5	3	195.6 ± 6.7	12.6 ± 0.3	25.9 ± 0.6	(3.5)	1.2×10^{43}
	1993.8	3	66.4 ± 3.0	4.1 ± 0.2	27.2 ± 1.1	(3.5)	4.4×10^{42}
C5	1984.2	3	34.7 ± 2.3	5.9 ± 0.8	0.8 ± 0.1	2.3	1.2×10^{43}
	1985.8	3	51.2 ± 3.0	3.1 ± 0.1	5.4 ± 0.2	3.3	6.1×10^{42}
	1987.3	3	80.7 ± 5.1	4.7 ± 0.2	6.6 ± 0.5	4.3	5.4×10^{42}
	1988.2	4	98.0 ± 4.0	5.4 ± 0.1	8.4 ± 0.4	5.0	4.5×10^{42}
	1989.2	3	28.1 ± 1.6	5.0 ± 0.9	0.7 ± 0.3	5.7	1.7×10^{42}
	1990.3	3	26.8 ± 1.1	4.9 ± 0.6	0.7 ± 0.2	6.0	1.4×10^{42}
	1991.7	2	14.3 ± 1.2	1.1 ± 0.2	1.6 ± 1.1	5.7	6.6×10^{41}
	1992.5	3	9.2 ± 0.7	2.7 ± 0.9	0.4 ± 0.1	5.0	7.4×10^{41}
	1993.8	2	5.5 ± 0.6	1.7 ± 0.7	0.4 ± 0.2	2.8	1.4×10^{42}
C4	1981.5	2	71.3 ± 4.4	3.7 ± 0.1	11.6 ± 1.4	3.2	7.4×10^{42}
	1982.4	2	162.7 ± 7.1	8.4 ± 0.3	12.5 ± 1.6	4.2	9.5×10^{42}
	1983.4	3	130.6 ± 6.4	6.8 ± 0.1	13.9 ± 0.5	4.7	5.6×10^{42}
	1984.2	2	113.2 ± 6.2	5.8 ± 0.1	12.3 ± 1.1	4.4	6.0×10^{42}
	1985.8	3	36.3 ± 3.0	1.9 ± 0.1	9.7 ± 0.6	4.2	2.3×10^{42}
	1987.3	2	22.1 ± 1.5	5.6 ± 2.1	0.5 ± 0.1	5.5	1.5×10^{42}
	1988.2	3	12.2 ± 0.8	0.7 ± 0.1	4.8 ± 0.8	7.2	3.1×10^{41}
	1989.2	2	43.3 ± 2.8	4.2 ± 1.0	1.9 ± 0.7	9.6	7.5×10^{41}
	1990.3	2	6.7 ± 1.4	2.7 ± 0.8	0.7 ± 0.1	12.2	1.3×10^{41}
	1991.7	2	8.0 ± 0.8	0.8 ± 0.5	1.4 ± 1.0	14.9	5.7×10^{40}
	1992.5	3	15.7 ± 1.2	1.7 ± 0.5	1.3 ± 0.5	14.2	1.3×10^{41}
	1993.8	2	12.4 ± 1.3	0.7 ± 0.1	4.1 ± 2.1	9.8	1.7×10^{41}

(continued on the next page)

Table 4.7: (continued)

(1) Name	(2) τ_ν	(3) N_ν	(4) S_{int}	(5) S_m	(6) ν_m	(7) γ_{min}	(8) $L_{max}^{4-25\,GHz}\ h^{-2}$
C3	1979.3	2	36.3 ± 3.2	2.3 ± 0.1	4.6 ± 0.7	7.3	9.3×10^{41}
	1980.6	2	19.9 ± 1.1	7.7 ± 1.6	0.4 ± 0.1	6.4	1.1×10^{42}
	1981.5	3	22.5 ± 1.3	2.7 ± 0.2	1.3 ± 0.1	6.0	1.1×10^{42}
	1983.4	2	13.1 ± 0.7	3.7 ± 1.7	0.4 ± 0.1	5.6	8.6×10^{41}
	1984.2	2	10.1 ± 0.6	0.9 ± 0.1	1.7 ± 0.3	5.7	4.9×10^{41}
	1985.8	2	6.2 ± 1.5	0.8 ± 0.2	0.5 ± 0.1	6.2	5.8×10^{41}
	1988.2	2	8.3 ± 1.0	0.8 ± 0.2	1.5 ± 0.7	7.9	2.1×10^{41}
	1989.2	2	17.1 ± 1.2	0.9 ± 0.1	6.1 ± 3.2	8.9	2.5×10^{41}
	1992.5	2	8.2 ± 1.2	0.5 ± 0.1	4.8 ± 3.8	13.4	5.8×10^{40}
	1993.8	2	3.1 ± 1.4	0.4 ± 0.4	0.6 ± 0.5	15.7	2.2×10^{40}
C2	1979.3	2	13.1 ± 0.9	0.9 ± 0.3	3.5 ± 2.4	7.8	3.1×10^{41}
	1980.6	2	15.0 ± 1.1	0.9 ± 0.1	5.3 ± 1.2	8.2	2.9×10^{41}
	1981.5	3	16.9 ± 1.0	1.8 ± 0.1	1.3 ± 0.2	8.4	4.0×10^{41}
	1984.2	2	12.5 ± 0.8	0.8 ± 0.1	7.1 ± 1.6	9.1	1.9×10^{41}
	1989.2	2	10.7 ± 1.2	0.6 ± 0.1	5.3 ± 3.3	10.5	1.3×10^{41}

Notes: 1 – component name; 2 – multi frequency data set epoch; 3 – number of frequencies available for spectral fit; 4 – integrated 4–25 GHz flux, $\times 10^{-14}$ erg s^{-1} cm^{-2}; 5 – peak flux density, Jy; 6 – turnover frequency, GHz; 7 – minimum Lorentz factor; 8 – upper limit for 4–25 GHz luminosity, erg s^{-1}.

chrotron spectrum requires an exceptional homogeneity of multifrequency data. Multifrequency VLBA observations can provide two factors most important for the data homogeneity: a reliable a priori calibration and the possibility of quasi–simultaneous observations at different frequencies. In the absence of VLBA data, and for the primary purpose of testing the software, we had used three observations from 1992 made relatively close in time. In this section, we describe briefly the procedure, and present the first results from mapping the turnover frequency distribution.

4.4.1 The procedure

The procedure implemented for continuous spectral fitting utilizes the same method as the one used for the discrete fitting. The synchrotron spectral cutoffs are allowed to vary, and the best fit is achieved through minimizing the χ^2 parameter. Fitting is performed in every pixel; the flux errors are estimated from the noise level and flux gradients in the total intensity maps. The fitted values can be smoothed, using various bin sizes. The output of the procedure can be the turnover frequency distribution, the peak flux density distribution, the integrated flux distribution, or *total intensity map* at the given frequency. The last option allows us to estimate, from the spectral shape, the expected source structure at any frequency within the range of observing frequencies of the maps used for the spectral fitting.

4.4.2 The turnover frequency distribution

To test the continuous spectral fitting, we have chosen three VLBI epochs (1994.44, 1992.45, 1992.71 at 22.3, 5, and 8.4 GHz correspondingly). The large time separation between the map at 8.4 GHz and the other two maps is likely to introduce errors into the results of the fitting. Unfortunately, these errors will be caused by the proper motion of the jet components, and therefore cannot be corrected. In our inclusion of the 8.4 GHz map we rely on the argument that (as it was shown in Section 4.2.4) variations of the spectral parameters are dependent mostly on the flux distribution at higher frequencies.

All three maps were produced from data with the same *uv*–ranges, and convolved with a circular 1.2 mas beam. For both the map at 5 GHz and the map 8.4 GHz, corrections for the frequency dependent shift of the core position have been made. All maps were clipped at their actual noise levels so as to avoid inclusion of side lobes into the fitting.

The resulting turnover frequency distribution is plotted in Figure 4.18. The saturation level is chosen so that variations of the turnover frequency are visible in the extended jet. Inside the jet, there is seen a narrow longitudinal feature having higher turnover frequency. Because the turnover frequency is very sensitive to spectral variations, it is possible that the observed feature reflects the location of an ultrarelativistic plasma pervading a thermal outflow (a *relativistic channel*, see Roland and Pelletier 1989). The transversal feature to the South of the channel coincides with the position

Table 4.8: Parameters of the VLBA maps

1	2	3	4	5	6	7	8
ν_{obs} [GHz]	S_{tot} [Jy]	S_{peak} [Jy/bm]	S_{neg} [Jy/bm]	S^{est}_{noise} [mJy]	Beam [mJy]	uv-range [Mλ]	uv-taper [Mλ]
22.2	7.210	4.138	-0.015	4.4±0.6	0.75×0.63, 9.°3	0-574	150
15.3	7.321	4.439	-0.015	3.9±0.4	0.84×0.68, 5.°5	0-440	150
8.4	7.607	4.173	-0.007	2.4±0.2	1.16×0.87, −20.°3	0-240	150
5.0	7.103	3.803	-0.018	4.1±0.9	1.57×1.20, −4.°1	0-150	150

Notes: 1 – observing frequency; 2 – total CLEAN flux; 3 – peak flux density; 4 – minimum flux density; 5 – measured noise; 6 – major axis, minor axis, and position angle of the tapered beam; 7 – uv-range of the data; 8 – half-power taper size.

of C5, and may reflect the location of the shock front in this component. However, reliability of the data used for the spectral fitting does not allow us to rule out a possibly spurious nature of the detected features in the jet. We expect further VLBA studies to clarify this issue.

The stability of the applied procedure of spectral fitting can be demonstrated by using this procedure for estimating the expected VLBI structure at some frequency which is not present among the actual data used for the fitting. We calculate the expected structure at 15 GHz and plot the corresponding map in Figure 4.19, together with the three actual VLBI maps at 5, 8.4, and 22.3 GHz.

Structure seen in the simulated 15 GHz map is consistent with the other three maps: the jet follows the same path; C5 is clearly visible, emission from C4 can be traced. We have produced several simulated maps at various frequencies between 5 and 22 GHz, using the spectral fitting software. All of them contain the features observed in the real maps, providing an argument for reliability of the spectral fitting procedure.

4.4.3 Turnover frequency map of 3C 345

The turnover frequency procedure was applied to the multifrequency VLBA observation of 3C 345 made on June 24, 1995. The source was observed at 5, 8.4, 15.4, and 22.2 GHz. The data were taken in the quasi-snapshot mode, with rotating frequencies. Thus, at each frequency, there was roughly one 5 minute scan made every 20 minutes. After the correlation, the data were fringe-fitted and mapped in AIPS and Difmap. In good agreement with the prediction made in Section 4.2.2, the sensitivity of the maps is roughly about 75% of the sensitivity of the single-frequency VLBI maps at corresponding frequencies. The main properties of the VLBA maps are given in Table 4.8. The maps are shown in Figure 4.20

The data were tapered at 150 Mλ, and the maps were produced with a circular restoring beam of 1.2 mas in diameter. The core shift was applied to the data at 5,

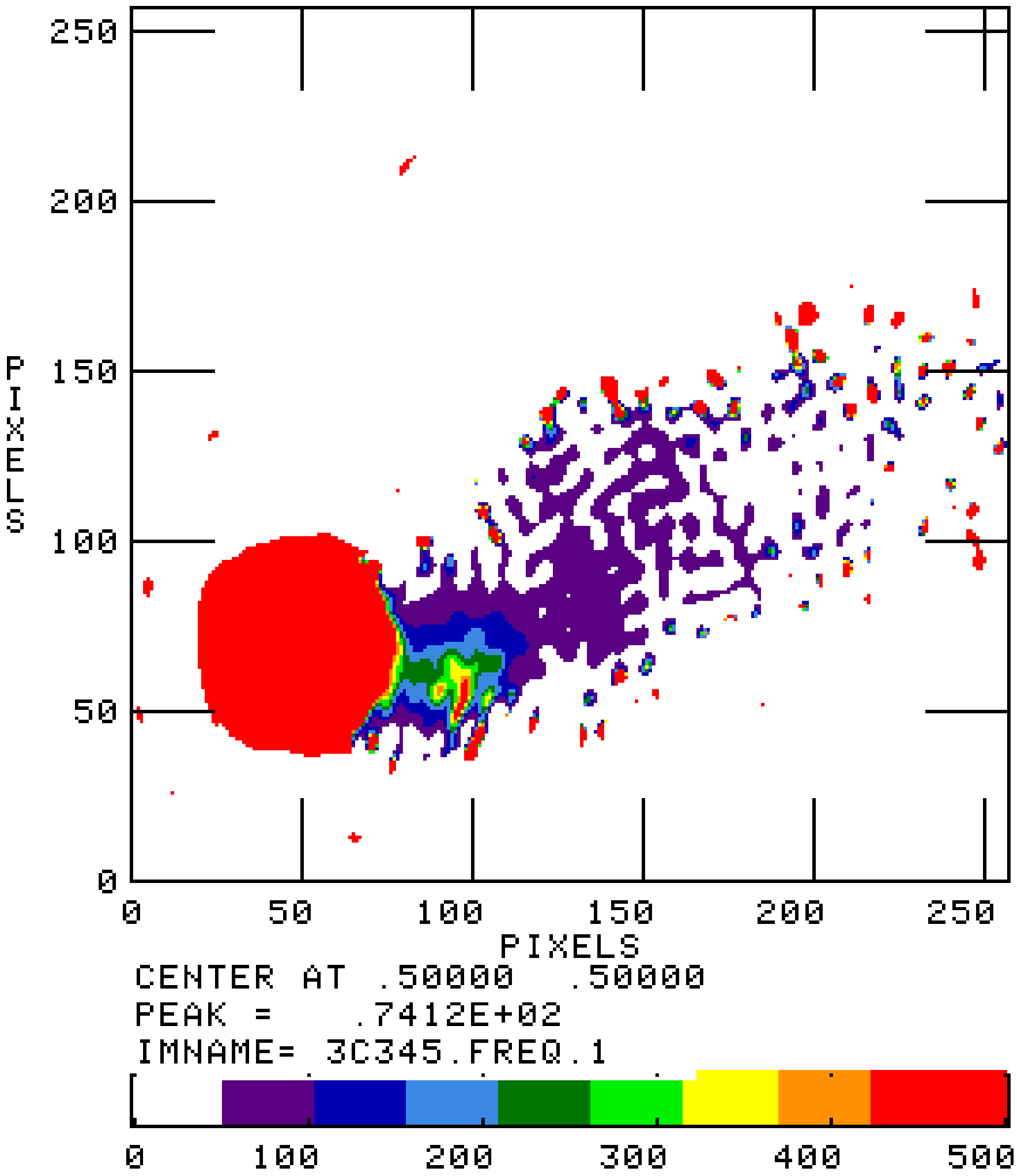

Figure 4.18: The turnover frequency distribution map obtained from continuous spectral fitting. The turnover frequency in the core is above the chosen saturation level (≈ 0.5 GHz). A narrow channel of higher turnover frequency is seen in the jet. The transversal feature to the South of the channel coincides with the location of C5, and may represent the shock front.

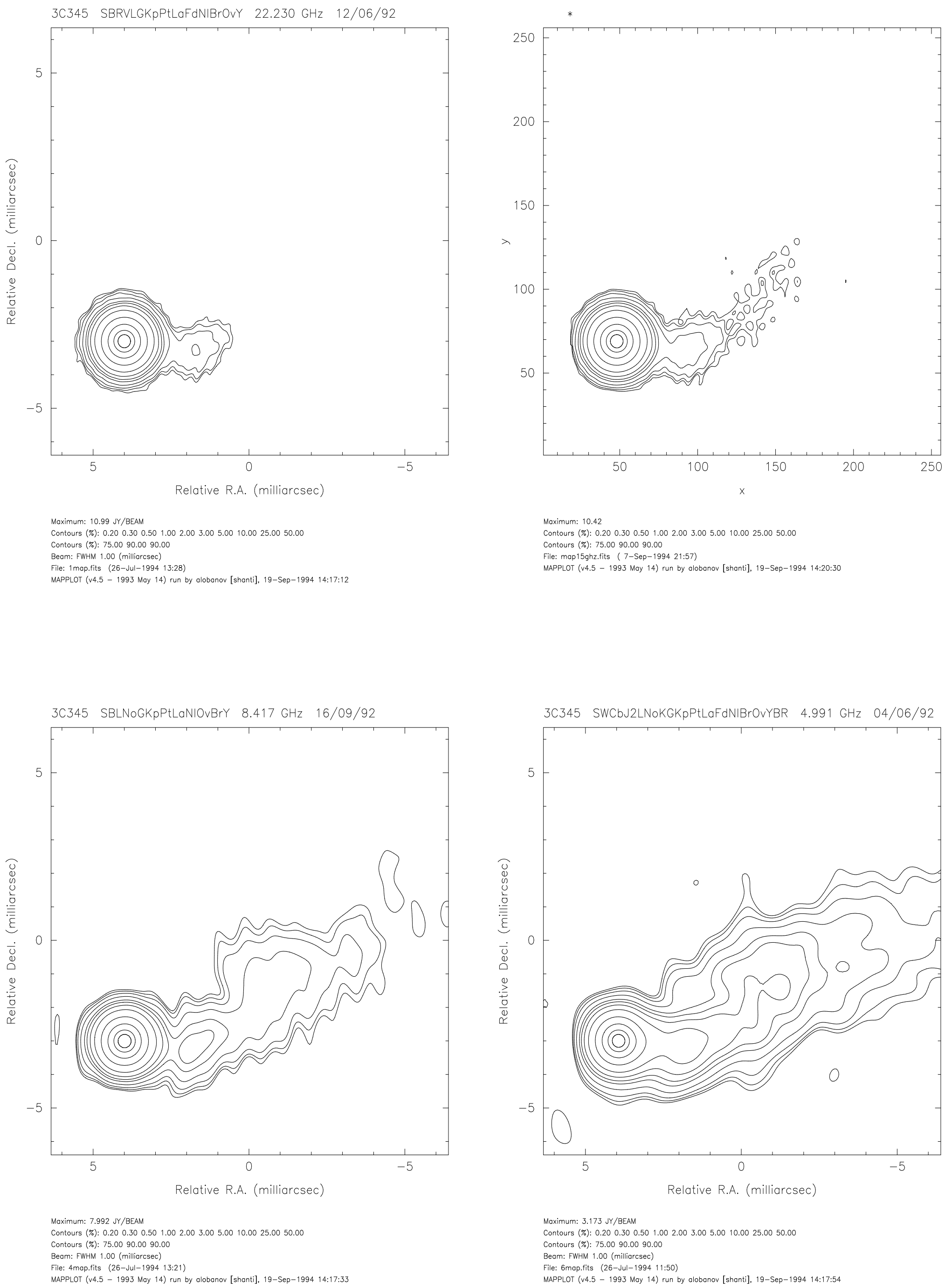

Figure 4.19: VLBI maps (22.3 GHz: top left; 8.4 GHz: bottom left; 5 GHz: bottom right) and a map produced using spectral fits to every pixel of the actual maps (15 GHz: top right).

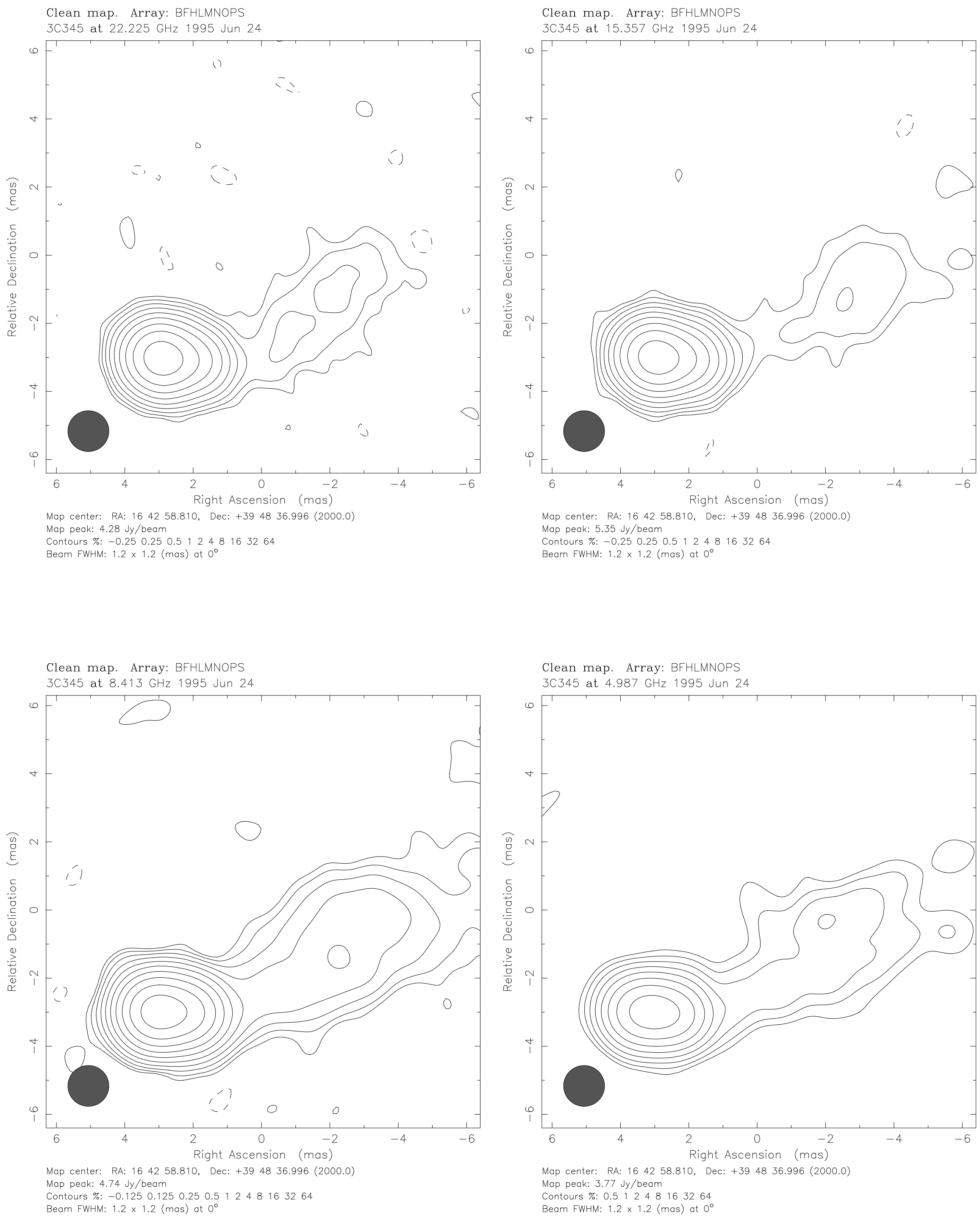

Figure 4.20: Maps of 3C 345 from the VLBA multifrequency data. The restoring beam is that used for the turnover frequency mapping.

8.4, and 15.4 GHz so as to give a common reference to the core position at 22.2 GHz. The magnitude of the core shift for the data at 15.4 GHz was determined from the fit described by Equation 4.3, whereas for the data at 5 and 8.4 GHz the measured values from Table 4.5 were used. The turnover frequency map produced from the maps shown in Figure 4.20 is shown in Figures 4.21 (the central part of the source) and 4.22 (the extended jet, with the central part being saturated). The saturation level in Figure 4.21 is 18 GHz.

There are two regions of higher turnover frequency seen in the top panel of Figure 4.21 that are extended in the direction transverse to the jet. These regions match the locations of the core and C7 fairly well. The increased turnover frequency may indicate that the emission is coming from a shocked plasma. The transverse extension is then consistent with strong shocks that are likely to be oriented almost perpendicularly to the jet direction. The lower panels of Figure 4.21 show profiles made along the horizontal line crossing the center of the core. The core (pixels -70 through -50), and C7 (pixels -35 through -15) are both visible in the turnover frequency profile. The turnover flux distribution is very smooth and peaks almost precisely at the center of the core. From the turnover frequency and turnover flux distributions, we can derive the profile of magnetic field in the central region using the relation for a plane shock (Cawthorne, 1991)

$$B(r) = C_0 \nu_m^5 r^4 S_m^{-2}, \tag{4.20}$$

where C_0 is the proportionality coefficicient. C_0 can be determined from the estimates of the absolute position and the magnetic field strength of the core observed at 22.2 GHz (see Section 6.3.1 of Chapter 6). The jet is assumed to have constant opening angle $\phi = 1^\circ$. Equation 4.20 expresses the magnetic field strength due to the compression that the plasma has undergone during shock formation. Therefore, the magnetic field also depends on the strength of the ambient magnetic field in the location of the jet where a shock is formed. We consider two cases, with the ambient magnetic field in the jet $B^1_{amb} \propto r^{-1}$, and $B^2_{amb} \propto r^{-2}$. Using the 22 GHz measurements from Table 6.1, we make an empirical estimate of C_0 for the abovementioned distributions of the ambient magnetic field. Formula 4.20 can be then rewritten for $B_{amb} \propto r^{-1}$ and r^{-2} respectively:

$$B_1(r) = 6.05 \cdot 10^{-3} \nu_m^5 r^3 S_m^{-2} \quad [G], \tag{4.21}$$

and

$$B_2(r) = 3.33 \cdot 10^{-2} \nu_m^5 r^2 S_m^{-2} \quad [G] \tag{4.22}$$

In these formulae, ν_m is in GHz, S_m is in Jy, and r is in parsecs. The resulting magnetic field profiles are plotted in the lower panels of Figure 4.21. The magnetic field rises sharply close to the outer edge of C7. This can signify the amount of plasma compression in the shock. The increasing magnetic field on the counterjet side (especially visible in the $B \propto r^{-2}$ profile) may reflect increasing electron plasma density near the jet origin. In the relativistic jets, the case $B \propto r^{-1}$ is expected to

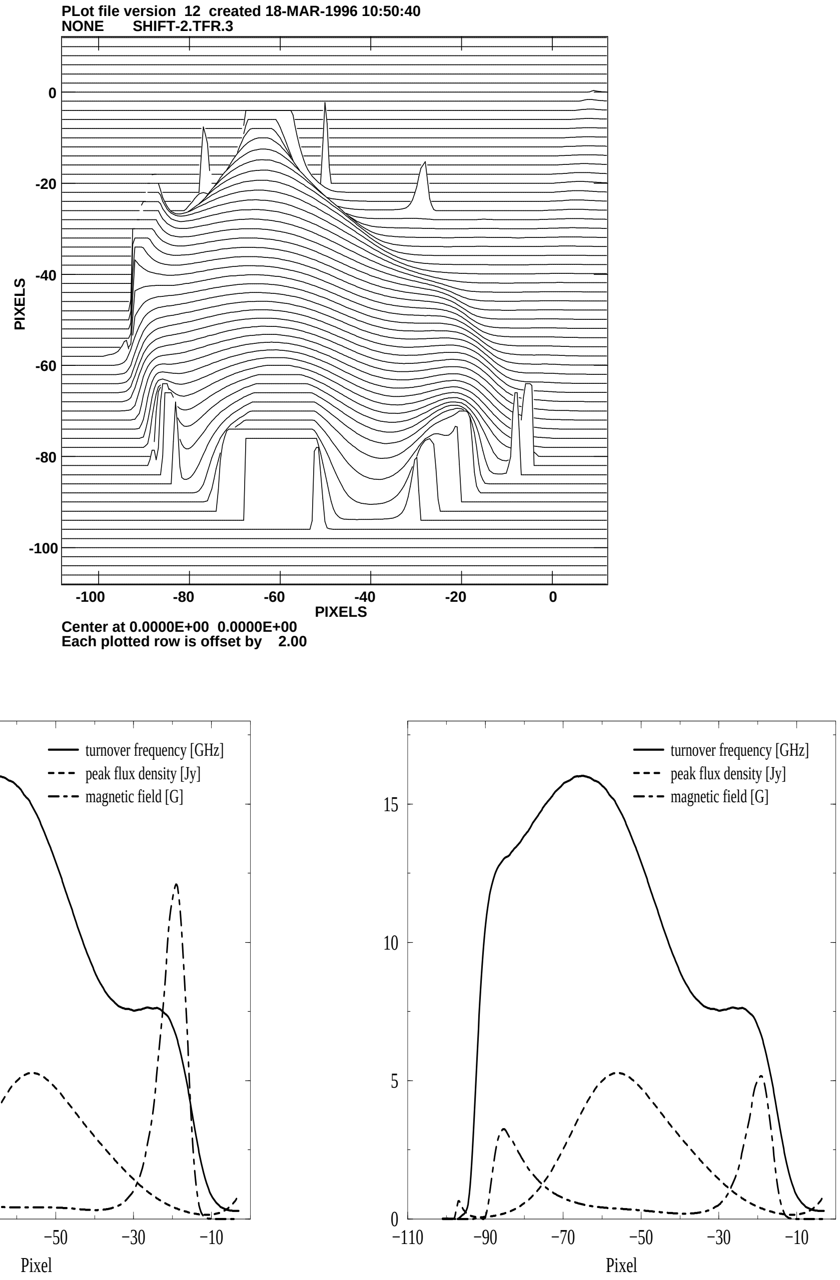

Figure 4.21: Upper panel: the turnover frequency distribution in the central part of 3C 345. The saturation level is at 18 GHz. The center of the core is in the pixel $(-60, -60)$. Lower panels: the profiles of turnover frequency, ν_m, turnover flux, S_m, and magnetic field, $B(r)$, along the line y=-60 crossing the center of the core. The ambient magnetic field decreases as r^{-1} (left panel), and r^{-2} (right panel).

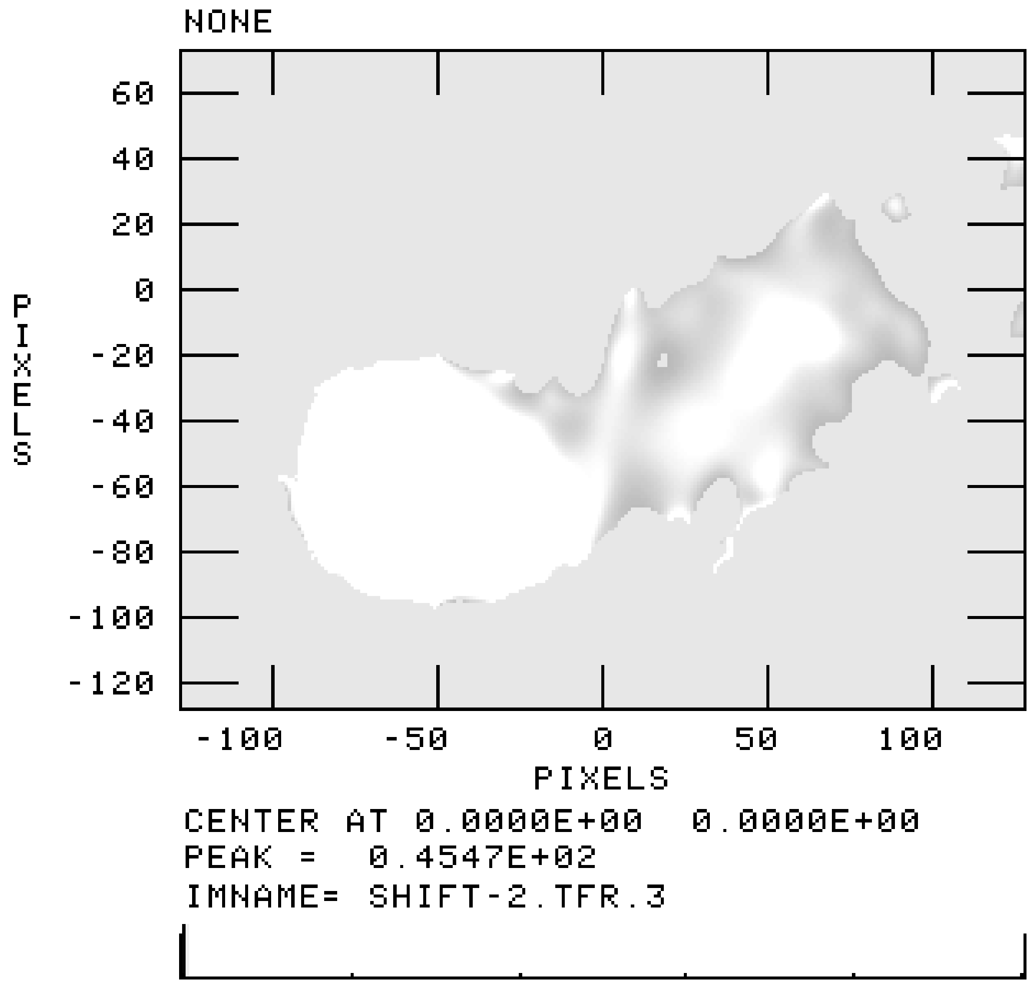

Figure 4.22: Turnover frequency distribution in the extended jet of 3C 345. The central region is saturated, for better representation of the turnover frequency variations in the jet.

be more likely. A somewhat high value of the magnetic field in C7 ($B_{C7}^{max} \approx 12\,$G) in this case might reflect possible errors in the estimates of the core magnetic field. However, the actual shape of the magnetic field profile is consistent with the shock models.

In the extended jet shown in Figure 4.22, the fitted values of the turnover frequency are lower than 5 GHz. Apparently, there are no strong shocks in these regions. Because the derived turnover frequency is too low, we cannot make statements about the physical conditions in the extended jet. Observations at lower frequencies (1.6, 1.4, 0.327 GHz) are required for better understanding the turnover frequency changes in these regions. With the available data, we can only make very general comments about the gradients observed in the turnover frequency map. The bright patterns elongated along the middle of the jet can be explained by the presence of an ultra-relativistic channel inside the jet. The tilted patterns seen in the jet resemble the patterns of Kelvin-Helmholtz instability (see Hardee *et al.* 1995, for the results from 3D simulations of the KH-instability driven jets). As has been noted above, the turnover frequency is exceptionally sensitive to the variations of plasma speed and density. Therefore, the observed patterns may reflect the velocity gradients and/or density gradients existing in the jet perturbed by the Kelvin-Helmholtz instability. However, the low frequency data are needed for making a better substantiated conclusion about the observed gradients of the turnover frequency.

4.5 Summary

In this chapter, we have covered several methodological and scientific aspects of studying synchrotron spectrum of the parsec–scale regions in AGN. The main conclusions are as follows:

1) We have discussed several techniques that can be used for obtaining spectral information from VLBI data: spectral index mapping, discrete and continuous broadband synchrotron spectrum fitting. A feasibility study shows that multifrequency VLBA observations can be used for spectral index mapping and continuous spectral fitting.

2) Spectral index maps of 3C345 are produced from VLBI data. The effect of frequency dependent shift of the core position is measured, and appropriate corrections are applied to the spectral index maps. The corrections are shown to be effective in decreasing the level of spurious features seen in spectral index maps.

3) A procedure developed for discrete and continuous broadband synchrotron spectrum fitting has been used for calculating the spectral parameters of the bright jet features. The turnover frequency, peak flux density, and integrated flux are calculated for the core and the jet components.

4) The first maps of the turnover frequency distribution are produced using continuous spectral fitting. The maps indicate possible locations of the relativistic channel and strong shock fronts inside the jet. The magnetic field distribution derived from

the turnover frequency and flux distributions is consistent with the plane shocks existing in the immediate vicinity of the source core. The extended emission appears to have a very low turnover frequency, for which we cannot give a good estimate, and can only deduce certain information about the gradients possibly existing in the extended regions. The observed gradients are consistent with the patterns of velocity distribution and density gradients found during mathematical simulations of relativistic jets. A more detailed study, with observations made at lower frequencies, is required for making conclusive statements about the nature of the observed gradients of the turnover frequency.